Ceramics International 44 (2018) 3775–3786

Contents lists available at ScienceDirect

Ceramics International

journal homepage: www.elsevier.com/locate/ceramint

Photoluminescent properties of the $Ba_{1-x}Zn_xMoO_4$ heterostructure obtained by ultrasonic spray pyrolysis

A.A.G. Santiago[a,*], C.R.R. Almeida[a], R.L. Tranquilin[a], R.M. Nascimento[a], C.A. Paskocimas[a], E. Longo[b], F.V. Motta[a], M.R.D. Bomio[a]

[a] LSQM, Laboratório de Síntese Química de Materiais - DEMat, Universidade Federal do Rio Grande do Norte - UFRN, P.O. Box 1524, 59078-970 Natal, RN, Brazil
[b] CDMF-UFSCar, Universidade Federal de São Carlos, P.O. Box 676, 13565-905 São Carlos, SP, Brazil

ARTICLE INFO

Keywords:
Ultrasonic spray pyrolysis
Barium molybdate
Zinc molybdate
Optical properties
Photoluminescence

ABSTRACT

In this study, $Ba_{1-x}Zn_xMoO_4$ (x = 0, 0.25, 0.5, 0.75 and 1) microspheres were the first time described in the literature the by ultrasonic spray pyrolysis method. Powders were characterized by X-ray diffraction (XRD), scanning electronic microscopy (SEM-FEG) and UV–visible and Photoluminescence (PL) spectroscopies. The XRD patterns showed that the samples with x = 0 and x = 1 displayed pure tetragonal and triclinic structures, respectively. On the other hand, samples with x = 0.25, 0.5 and 0.75 revealed the formation of tetragonal/triclinic heterojunction structure. The SEM-FEG images showed that the $Ba_{1-x}Zn_xMoO_4$ particles present the spherical morphology with the decrease of particle sizes when the value of "x" increase. The gap energies vary between 4.56 eV and 4.17 eV, being influenced by the degree of structural order-disorder. The PL emission spectra of the samples showed a broad band behavior with emission intensity predominant in the orange-red region and of a lower intensity in the blue-green region. The chromaticity coordinates x and y showed that the samples with $x \leq 0.75$ present emission in orange, while the samples with x = 1 showed emission in white.

1. Introduction

Molybdates have been the subject of research by their potential application in diverse fields such scintillators, photoluminescence, solid state lasers, optical fibers, microwave applications and photocatalysts [1–3]. Samdani et al. [4] studied the use of $FeMoO_4$ as an electrode material in biosensors to detect norepinephrine and showed excellent electrocatalytic performance of the $FeMoO_4$ in the oxidation of this norepinephrine. Wu et al. [5] showed that Er^{3+}-doped $YbMoO_4$ synthesized by the coprecipitation route has high thermal sensitivity and thus a great potential for the development of temperature sensors. Liao et al. [6] demonstrated in their work that NiMoO4 nanofibers sensors produced by the electrospining technique exhibit good catalytic activity regarding glucose embracing low response potential and high sensitivity. Kim et al. [7] investigated the dependence on microwaves dielectric properties of some molybdates with respect to the crystalline structure, bond character and electronic characteristics, verified that the dielectric constant (K) is affected mainly by the dielectric polarizabilities, molar volume and electronic oxide polarizabilities.

Barium molybdate ($BaMoO_4$) is one of the most important material, having a scheelite-type tetragonal structure, with a space group of I41/a and symmetry C_{4h}^6 [8,9]. The scheelite-type structure has a chemical formula ABO_4, where A cation has a tetrahedral coordination and B cation is the eight-coordinated by O^{2-}, being the lattice is formed by AO_8 dodecahedron and BO_4 tetrahedral connected in three dimensions [10]. On the other hand, zinc molybdate ($ZnMoO_4$) present different structures depending on its preparation conditions, usually in two phases α-$ZnMoO_4$ and β-$ZnMoO_4$ [11]. The α-$ZnMoO_4$ has triclinic structure and space group $P\bar{1}$ [12], where all zinc atoms are bonded to six oxygen atoms, generating distorted octahedral [ZnO_6] clusters and the molybdenum atoms are coordinated to four oxygen atoms, forming the tetrahedral [MoO_4] clusters [13]. The β-$ZnMoO_4$ has a wolframite-type monoclinic structure and space group P2/c, where both zinc and molybdenum atoms bonded to six oxygen atoms produced the distorted octahedral [ZnO_6]/[MoO_6] clusters, respectively [14].

Several properties have been exploited from barium molybdate and zinc molybdate. Ma et al. [15] studied the use of $BaMoO_4$ as anode material of lithium ion batteries (LIBs) and sodium ion batteries (SIBs), with high discharge capacity of 410 mA h g^{-1} after 900 cycles at 200 mA g^{-1} when used as anode material of LIBs and discharge capacity of 50 mA h g^{-1} after 100 cycles at 50 mA g^{-1} when used as anode material SIBs. Alencar et al. [16] used BaMoO4 prepared by the microwave-assisted hydrothermal method and polymeric precursor method as a solid catalyst for the oxidation reaction of toluene in its gas

* Corresponding author.
E-mail address: gsantiago.anderson@gmail.com (A.A.G. Santiago).

https://doi.org/10.1016/j.ceramint.2017.11.161
Received 24 October 2017; Received in revised form 20 November 2017; Accepted 22 November 2017
Available online 23 November 2017
0272-8842/ © 2017 Elsevier Ltd and Techna Group S.r.l. All rights reserved.

phase. Guo et al. [17] synthesized Shuttle-like BaMoO4 microcrystals and demonstrated experimentally and theoretically that this material has ferromagnetism at room temperature. Fei et al. [18], suggests that α-$ZnMoO_4$ nanoparticles offer a future alternative as an anode material for LIBs, because they have a high capacity stability of ~389.0 mA h g^{-1} at 50 mA g^{-1} with loss capacity of 0.2% per cycle from the second cycle. Several studies have been developed with $ZnMoO_4$ for applications in cryogenic scintillation bolometers because they are scintillating materials. Moreover, it is possible to observe extremely rare processes, such as neutrinoless double beta decay [12,19–21].

One of the most exploited property of molybdates is photoluminescence (PL), with several studies in the literature. Abreu et al. [22] studied the photoluminescent properties of $BaMoO_4$ and indicated the existence of an electronic order-disorder relationship in short and intermediate material ranges and shallow and deep defects in the surface of the structure with interfaces that fill additional levels in the band gap using the synthesis method. Sczancoski et al. [8] demonstrated significant difference in the PL spectra of $BaMoO_4$ when excited by two distinct wavelengths (350 nm and 488 nm) and attributed this phenomenon to the presence of oxygen 2p state located above the valence band and molybdenum 4d state situated near the conduction band. Hu et al. [23] synthesized $Ba_xZn_{1-x}MoO_4:Eu^{3+}$ ($0.1 \leq x \leq 0.7$) by the solid-state reaction method and investigated the PL properties and observed that a Ba^{2+} increase could increase the PL intensity, obtaining excellent red light emission. Zhai et al. [24] showed $ZnMoO_4$ nanowires exhibit a green emission band in PL spectrum and suggest that defects such as oxygen vacancies, zinc vacancies, interstitials oxygen and interstitials zinc are responsible for this emission.

In order to obtain these several properties and applications of the molybdates, the use of different synthesis methods is critical. Several studies described in the literature shown the synthesis of $BaMoO_4$ and $ZnMoO_4$ using methods that exhibit drawback such as high temperatures, long periods of time, use of expensive reagents (surfactants), and/or non-continuous routes. Thus, the synthesis routes that are being used to obtain $BaMoO_4$ and $ZnMoO_4$ are Czochralski technique [19,20,25], solid state reaction [26,27], sol-gel [28,29], coprecipitation [30–32], biomineralization [33], electrochemical [34], hydrothermal [13,35,36], microwave-assisted hydrothermal [22,37] and sonochemical [38,39].

Recently, the ultrasonic spray pyrolysis (USP) method has been used to produce different material types with spherical shape particles without using surfactants [40–48], being a low cost method, easy, one-step and continuous process to obtain materials with high purity, non-agglomerated powders with homogeneous morphological quality and with time of formation of the particles inside reactor in about 1 min [46,49,50]. The particle size and particle size distribution vary according to parameters such as atomizing frequency, carrier gas flow rate, pyrolysis temperature and the precursor solution concentration [51]. The precursor solution is generally easy to obtain, consisting of an aqueous solution containing dissolved reagents, such as nitrates, acetates, chlorides and ammonium [52–54].

In this study, $Ba_{1-x}Zn_xMoO_4$ (x = 0, 0.25, 0.5, 0.75 and 1) microspheres were prepared, in one-step, the by ultrasonic spray pyrolysis method using temperatures of 1000 °C and 1100 °C during 1 min, being first time described in the literature. The structure, morphology and optical properties of $Ba_{1-x}Zn_xMoO_4$ are investigated.

2. Experimental

2.1. Materials

Barium nitrate ($Ba(NO_3)_2$; 99.0% purity; Vetec), zinc nitrate ($Zn(NO_3)_2{\cdot}6H_2O$; Synth), molybdic acid (H_2MoO_4; 85% purity; Alfa Aesar), citric acid anhydrous ($C_6H_8O_7$; 99.5 purity; Synth) and distilled water were used as reagentes to prepared the $Ba_{1-x}Zn_xMoO_4$.

Table 1
The samples codes table.

x ($Ba_{1-x}Zn_xMoO_4$)	Temperature (°C)	Code
x = 0	1000	BMO10
x = 0	1100	BMO11
x = 0.25	1000	BZ25MO10
x = 0.25	1100	BZ25MO11
x = 0.5	1000	BZ5MO10
x = 0.5	1100	BZ5MO11
x = 0.75	1000	BZ75MO10
x = 0.75	1100	BZ75MO11
x = 1	1000	ZMO10
x = 1	1100	ZMO11

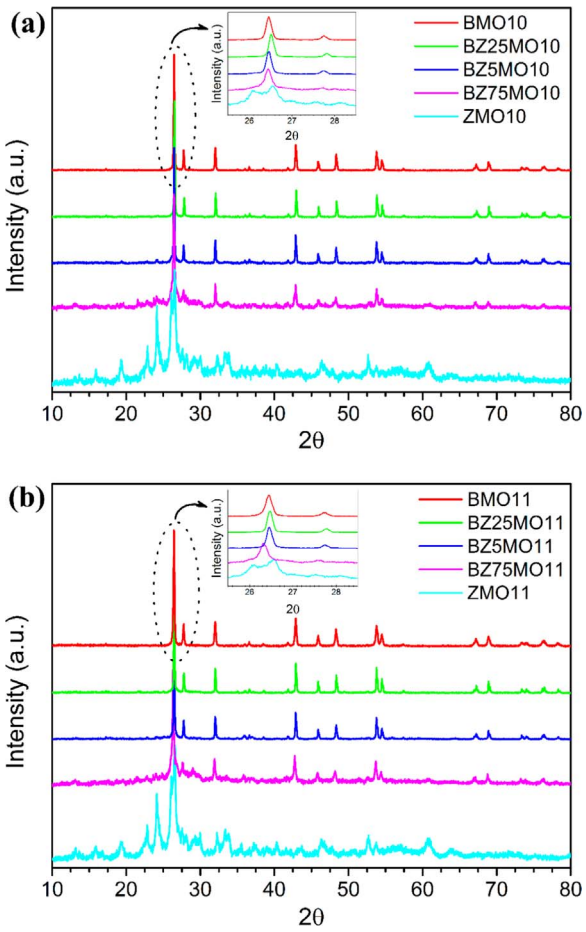

Fig. 1. XRD patterns of $Ba_{1-x}Zn_xMoO_4$ (x = 0, 0.25, 0.5, 0.75 and 1) obtained by USP at (a) 1000 °C and (b) 1100 °C.

2.2. Preparation of $Ba_{1-x}Zn_xMoO_4$ particles

The $Ba_{1-x}Zn_xMoO_4$ (x = 0, 0.25, 0.5, 0.75 and 1) powders were prepared using method ultrasonic spray pyrolysis [50,55]. To prepare $Ba_{1-x}Zn_xMoO4$ with x = 0, the precursor solution was prepared dissolving 0.04 mol of citric acid anhydrous, 6.728 mmol of molybdic acid and 6.728 mmol of barium nitrate in 100 ml of distilled water. The precursor solution was atomized using an ultrasonic nebulizer with 2.4 MHz of frequency. The laminar flow reactor of the aerosol used was a 50 mm diameter quartz tube with 1.1 m of length, which was inserted into a tubular horizontal electric furnace of double heat zone. The rate air flow used was of 3 L min^{-1}. The sprayed droplets were transported by means of the reactor, heated by the tubular electric furnace and transformed into solids particles inside the reactor. The resultant particles were collected by means of electrostatic precipitation in the

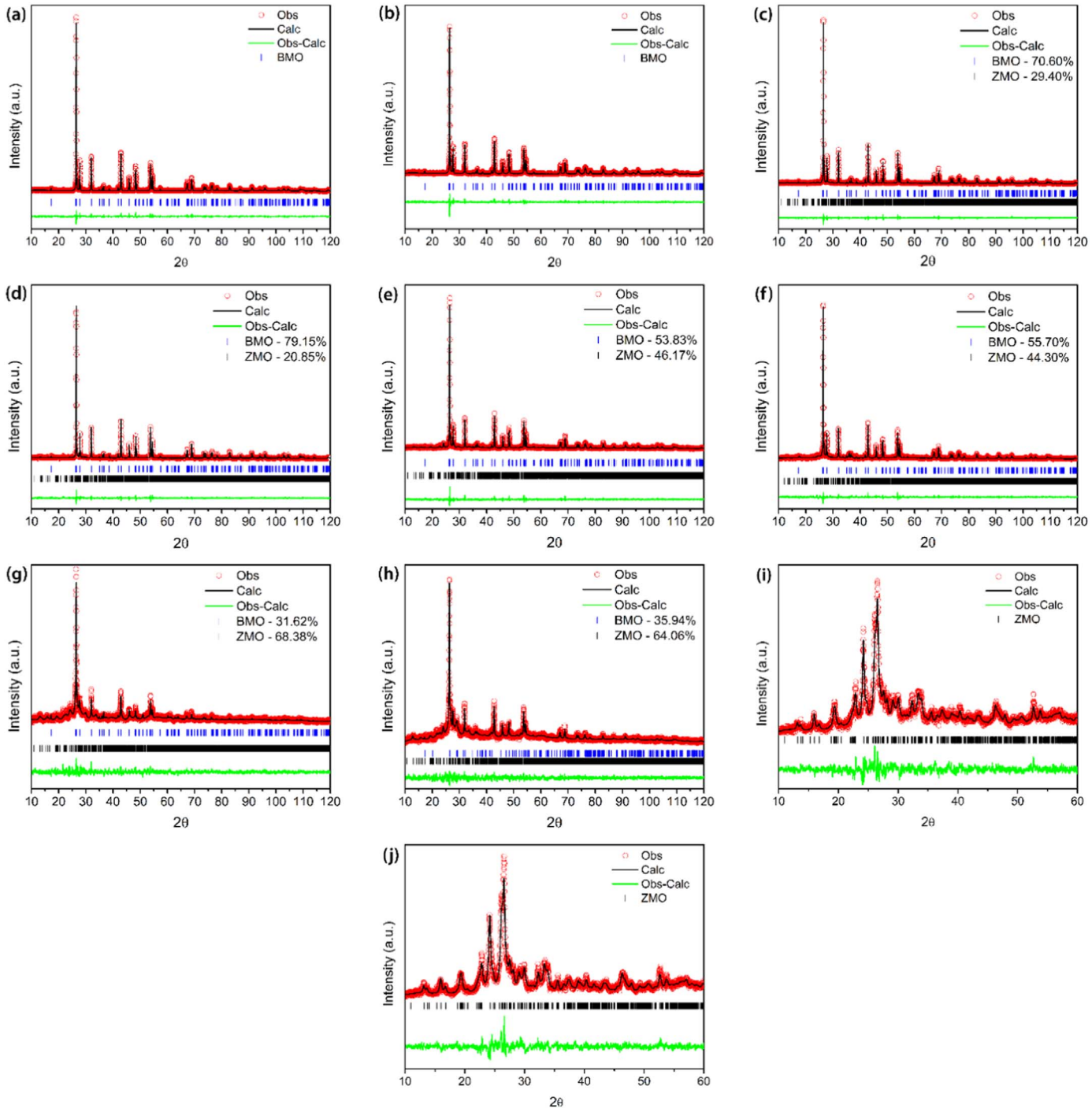

Fig. 2. Rietveld refinement of (a) BMO10, (b) BMO11, (c) BZ25MO10, (d) BZ25MO11, (e) BZ5MO10, (f) BZ5MO11, (g) BZ75MO10, (h) BZ75MO11, (i) ZMO10 and (j) ZMO11.

reactor exit by a copper tube. The temperatures used for heat treatment were: 600 °C at zone 1 and; 1000 °C and 1100 °C at zone 2 in the tubular electric furnace. Considering the drag flow of the reactor, the residence time of the particles inside the reactor was approximately 1 min. The other precursors solutions (x = 0.25, 0.5, 0.75 and 1) were realized according to stoichiometry. Table 1 shows the sample codes.

2.3. Characterization of $Ba_{1-x}Zn_xMoO_4$ particles

$Ba_{1-x}Zn_xMoO_4$ powder, with x = 0, 0.25, 0.5, 0.75, and 1, was characterized by XRD using a Bruker diffractometer, D2 Phaser model with CuKα radiation (λ = 1.5406 Å), 30 kV and 30 mAh, 2θ from 10° to 80° and the step speed of $1^{\circ}min^{-1}$. For the Rietveld refinement measurement, it was used 2θ range from 10° to 120° and step size of $0{,}02^{\circ}\ min^{-1}$. The morphologies were investigated using a field-emission gun scanning electron microscopy (FEG-SEM; Carl Zeiss, Supra 35-VP Model, Germany) operated at 6 kV. The Uv–visible reflectance spectra of the powders were performed using a Shimadzu spectrophotometer, UV-2600 model. Photoluminescence (PL) spectra were obtained using a Thermal Jarrell-Ash Monospec 27 monochromator and Hamamatsu R446 photomultiplier. A laser was used as the excitation source on the samples at a wavelength of 350.7 nm with krypton ions (Coherent Innova) with an output of approximately 13.3 mW. All measurements were taken at room temperature.

Table 2
Rietveld refined structural parameters for the $Ba_{1-x}Zn_xMoO_4$ with x = 0, 0.25, 0.5, 0.75 and 1.

Compounds	BMO10	BMO11	BZ25MO10	BZ25MO10	BZ25MO11	BZ25MO11
Crystal system	Tetragonal	Tetragonal	Tetragonal	Triclinic	Tetragonal	Triclinic
Space Group	$I4_1/a$	$I4_1/a$	$I4_1/a$	*P-1*	$I4_1/a$	*P-1*
Lattice parameters (Å)						
a	5.5813	5.5825	5.5814	6.9790	5.5823	7.0075
b	–	–	–	8.3340	–	8.2855
c	12.8313	12.8374	12.8269	9.6380	12.8258	9.6798
c/a	2.2990	2.2996	2.2981	–	2.2976	–
α	90°	90°	90°	96.420°	90°	96.184°
β	–	–	–	106.200°	–	106.606°
γ	–	–	–	102.050°	–	101.845°
V(Å³)	399.6986	400.0687	399.5842	517.7519	399.6784	518.7600
X^2	0.866	0.822	0.840	0.840	0.902	0.902
Rwp (%)	14.88	15.51	13.97	13.97	14.76	14.76
Rp (%)	10.94	11.69	10.19	10.19	10.87	10.87
D (nm)	600.09	590.95	648.52	210.88	632.24	234.04
ε $(x10^{-3})$	0.445	1.258	0.605	6.334	0.269	3.501
Compounds	BZ5MO10	BZ5MO10	BZ5MO11	BZ5MO11	BZ75MO10	BZ75MO10
Crystal system	Tetragonal	Triclinic	Tetragonal	Triclinic	Tetragonal	Triclinic
Space Group	$I4_1/a$	*P-1*	$I4_1/a$	*P-1*	$I4_1/a$	*P-1*
Lattice parameters (Å)						
a	5.5820	6.9658	5.5815	6.9820	5.5806	6.9615
b	–	8.3715	–	7.6498	–	8.4506
c	12.8344	9.6859	12.8345	9.9326	12.8655	9.6939
c/a	2.2992	–	2.2995	–	2.3054	–
α	90°	96.554°	90°	99.286°	90°	96.886°
β	–	107.031°	–	104.178°	–	106.816°
γ	–	101.754°	–	101.824°	–	101.636°
V(Å³)	399.9007	519.4929	399.8335	490.7500	400.6787	524.8600
X^2	0.874	0.874	1.022	1.022	1.091	1.091
Rwp (%)	14.63	14.63	14.56	14.56	15.47	15.47
Rp (%)	11.17	11.17	10.88	10.88	11.93	11.93
D (nm)	602.02	195.42	561.13	171.93	329.35	72.07
ε $(x10^{-3})$	0.587	5.233	0.561	1.017	0.343	0.075
Compounds	BZ75MO11	BZ75MO11	ZMO10	ZMO11		
Crystal system	Tetragonal	Triclinic	Triclinic	Triclinic		
Space Group	$I4_1/a$	*P-1*	*P-1*	*P-1*		
Lattice parameters (Å)						
a	5.5832	6.8384	6.9714	6.9719		
b	–	8.7036	8.3904	8.3981		
c	12.8568	9.6496	9.7040	9.6990		
c/a	2.3027	–	–	–		
α	90°	96.064°	96.864°	96.826°		
β	–	106.985°	106.912°	106.972°		
γ	–	104.587°	101.804°	101.817°		
V(Å³)	400.7809	521.4500	521.7799	521.8716		
X^2	0.902	0.864	0.854	0.864		
Rwp (%)	12.19	11.48	10.78	11.48		
Rp (%)	9.24	9.02	8.49	9.02		
D (nm)	308.53	113.82	159.02	151.77		
ε $(x10^{-3})$	0.320	1.608	0.160	0.153		

3. Results and discussion

3.1. X-ray diffraction

Fig. 1 show the XRD spectra of samples $Ba_{1-x}Zn_xMoO_4$ (x = 0, 0.25, 0.5, 0.75 and 1) with temperature of 1000 °C and 1100 °C. Samples with x = 0, 0.25, 0.5 and 0.75 were indexed in a unit cell with tetragonal scheelite structure with space group *I41/a* (88) according to letter JCPDS 29-0193. While the samples with x = 1 were indexed in a unit cell with triclinic structure with the space group *P*-1 (2) according to letter JCPDS 35-0765. The samples with x = 0 and 0.25 showed no traces of additional peaks, thus confirming a BMO single phase. The samples with x = 0.5 and 0.75 showed the presence of small additional peaks, demonstrating the formation of a heterostructure. In samples with x = 1 were not detect the presence of additional peaks, indicating pure samples of ZMO.

The Rietveld refinement method [56] was used to explain possible differences in the structural arrangements induced by the processing of $Ba_{1-x}Zn_xMoO_4$ particles. The General Structure Analysis System (GSAS) program with the EXPGUI graphical interface [57] was used to perform the refinement. The refined parameters were: scaling factor and phase fraction; background, which was modeled using a displaced Chebyshev polynomial function; peak shape, which was modeled using Thomson-Cox-Hasting pseudo-Voigt; change in lattice constants; fractional atomic coordinates; and isotropic thermal parameters. The results of the Rietveld refinement are shown in Fig. 2.

For samples with x = 0 the diffraction patterns are well matched to ICSD 50821 (BMO) and for x = 1 to ICSD 411378 (ZMO). However, for the samples with x = 0.25, 0.5 and 0.75 the diffraction patterns are well adapted to ICSD 50821 (BMO) and ICSD 411378 (ZMO), indicating the formation of a heterostructure. In general, the differences between the experimentally observed XRD patterns and the theoretically calculated data are close to zero, as shown in the Obs-Calc line. The refinement results are summarized in Table 2 and more details are provided in the Support information (Table S1).

Table 2 shows low deviations of the reliability parameters X^2, Rwp and Rp, indicating good quality of structural refinements and numerical results. These data confirm that the $Ba_{1-x}Zn_xMoO_4$ samples with x = 0

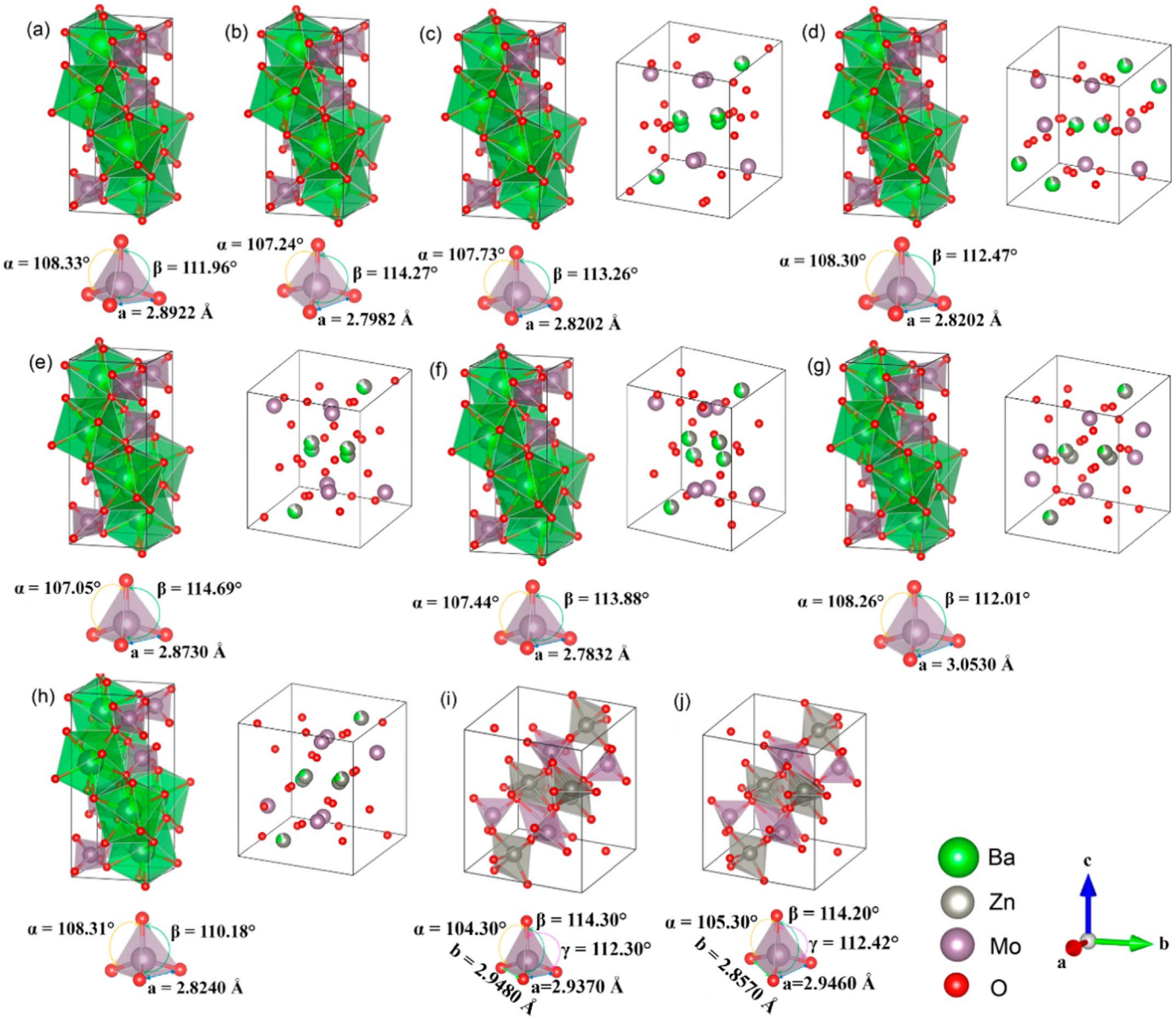

Fig. 3. Model of tetragonal structure of the (a) BMO10 and (b) BMO11; tetragonal and triclinic structure of the (c) BZ25MO10, (d) BZ25MO11, (e) BZ5MO10, (f) BZ5MO11, (g) BZ75MO10 and (h) BZ75MO11; and triclinic structure of the (i) ZMO10 and (j) ZMO11.

are isostructural, with crystal structure being suitably described by a tetragonal scheelite structure, with symmetry described by space group I41/a. The samples with x = 1 are also isostructural, but having a crystal structure adequately described by a triclinic structure, with symmetry described by the space group *P*-1. On the other hand, the samples with x = 0.25, 0.5 and 0.75 are heterostructural, being described by a tetragonal scheelite structure, with symmetry described by space group I41/a; and a triclinic structure, with symmetry described by the space group *P*-1.

When x = 0.25, 0.5 and 0.75, the changes in the network parameters and intensity of diffraction peaks are related to the atomic substitution in the structure, temperature, change of synthesis and heterostructural formation, which cause expansion or contraction at the atomic distances of the unit cell. In our work, the atomic substitution of the Ba^{2+} atoms by the smaller Zn^{2+} atoms, which have an ionic radius of 0.142 nm and 0.090 nm, respectively [58]. Generally, this type of substitution is expected to result in the decrease of the network parameters of the unit cell, which is not perceived according to Table 2. This phenomenon can be understood by the solubility difference between barium molybdate and zinc. As zinc molybdate has lower solubility than barium molybdate, zinc molybdate will form first than barium molybdate. Thus, Ba^{2+} atoms will be arranged within the triclinic structure of the zinc molybdate. Subsequently, during the formation of barium molybdate, Zn^{2+} atoms will be arranged within the tetragonal structure. Therefore, eventually, there is the formation of a tetragonal/triclinic heterostructure containing atomic substitutions in both structures. It is noticed that the formation percentage of each structure follows values close to stoichiometric ones. However, with the increase in temperature there is an increase in the percentage of the tetragonal structure, which probably occurs because of the rearrangement of the triclinic structure for the tetragonal structure. The formation of this heterostructure will cause distortions in the Ba-O, Zn-O and Mo-O bonds, consequently, in the distortions suffered in the clusters of $[BaO_8]/[ZnO_8]$, $[ZnO_6]/[BaO_6]$ and/or $[MoO_4]$. From the atomic coordinate data and lattice parameters obtained in the refinement (Table 2 and S1), the VESTA program [59] was used to model the unit cells of each sample, as shown in Fig. 3.

For the samples with x ≤ 0.75, with the increase of the substitution

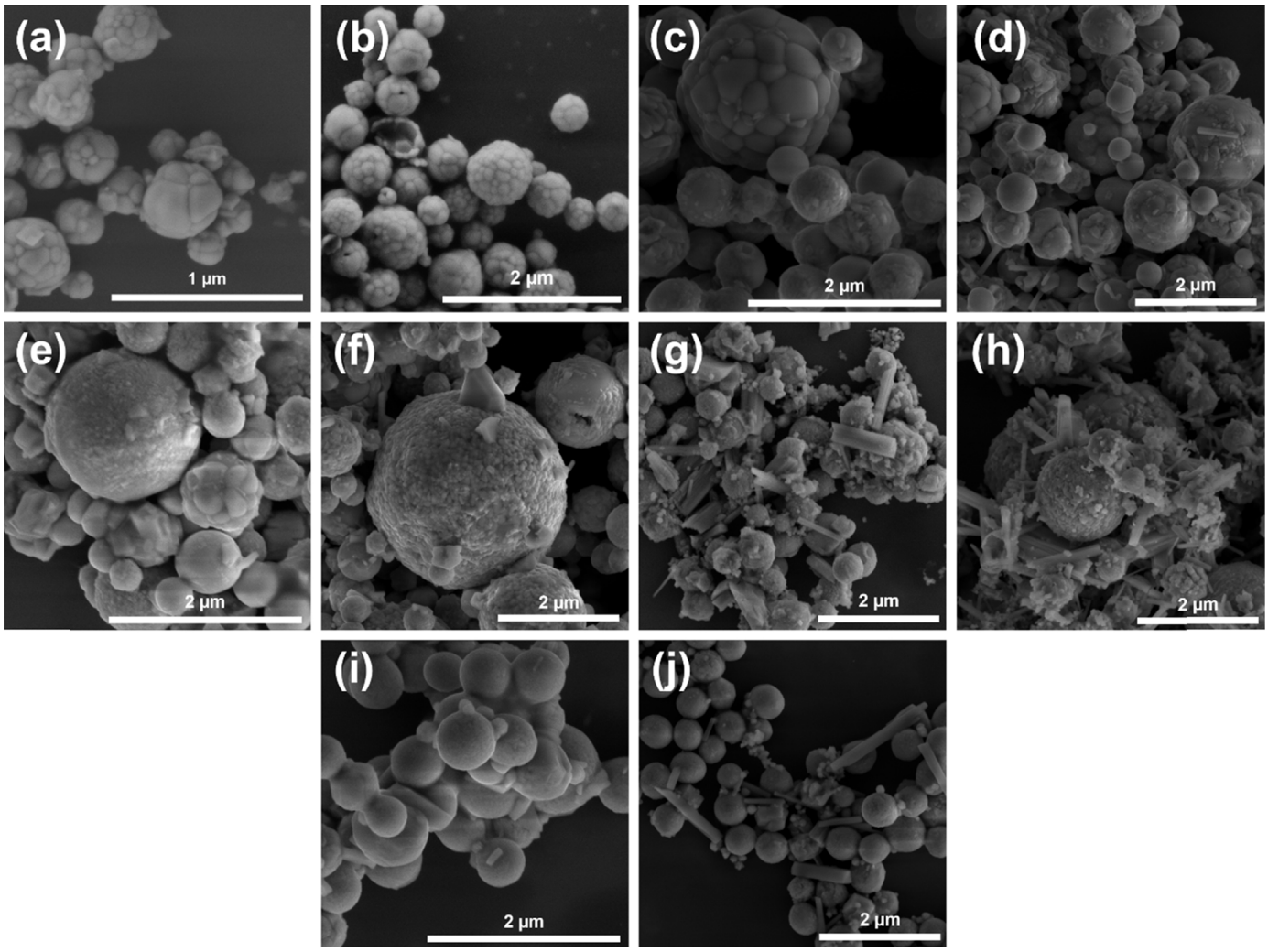

Fig. 4. SEM micrographs of (a) BMO10, (b) BMO11, (c) BZ25MO10, (d) BZ25MO11, (e) BZ5MO10, (f) BZ5MO11, (g) BZ75MO10, (h) BZ75MO11, (i) ZMO10 and (j) ZMO11.

Table 3
Average diameter of the particles of $Ba_{1-x}Zn_xMoO_4$ (x = 0, 0.25, 0.5, 0.75 e 1) obtained by the method USP.

Sample	BMO10	BZ25MO10	BZ5MO10	BZ75MO10	ZMO10
Mean (nm)	786 ± 273	610 ± 185	729 ± 256	637 ± 173	522 ± 136
Sample	BMO11	BZ25MO11	BZ5MO11	BZ75MO11	ZMO11
Mean (nm)	546 ± 145	655 ± 200	669 ± 232	661 ± 173	535 ± 113

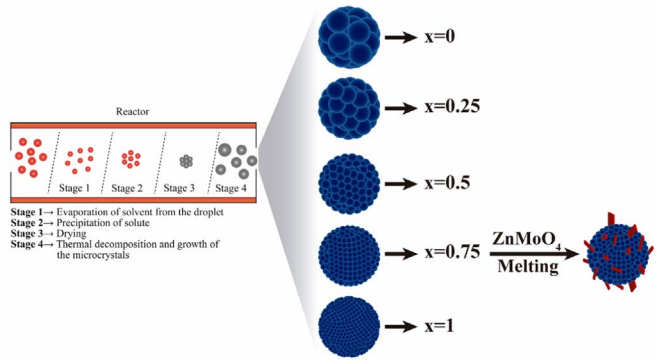

Fig. 5. Illustration of the variation of the size of the primary particles in the formation of the adjacent particles with the change of the precursor reagent.

of the Ba^{2+} atoms for the Zn^{2+} atoms, it is noticed changes in the distortion of the [BaO_8], [ZnO_6] and/or [MoO_4] clusters. In the tetrahedral clusters of [MoO_4], there are distortions at the bonding angles of the O-Mo-O atoms and a change in the length of the edge of the base of the tetrahedron, which occurs due to the increase of x and the increase of the synthesis temperature. For samples with x = 1, distortions in the clusters of [ZnO_6] and/or [MoO_4] are promoted by an increase in the temperature. In the tetrahedral clusters of [MoO_4] there are distortions at the bonding angles of the O-Mo-O atoms and a change in the length of the edges forming the base of the tetrahedron.

3.2. Scanning electron microscope

Fig. 4 shows SEM-FEG micrographs of the samples of $Ba_{1-x}Zn_xMoO_4$ (x = 0, 0.25, 0.5, 0.75 and 1) synthesized at a temperature of 1000 °C and 1100 °C. Table 3 shows the mean particle diameter values of each sample and Fig. S2 shows histograms of the particle diameter distribution.

The particles obtained in this work by the process of ultrasonic spray pyrolysis have spherical morphology, predominantly with diameters ranging from 100 nm to 1500 nm. Fig. 4a and b depict the $BaMoO_4$ microspheres formed by the USP process at 1000 °C and 1100 °C. It can be observed that the microspheres have well defined contours between the primary particles which form the microsphere. However, for the complete formation of such microparticles, it is required the union of few primary particles with large particle size. On

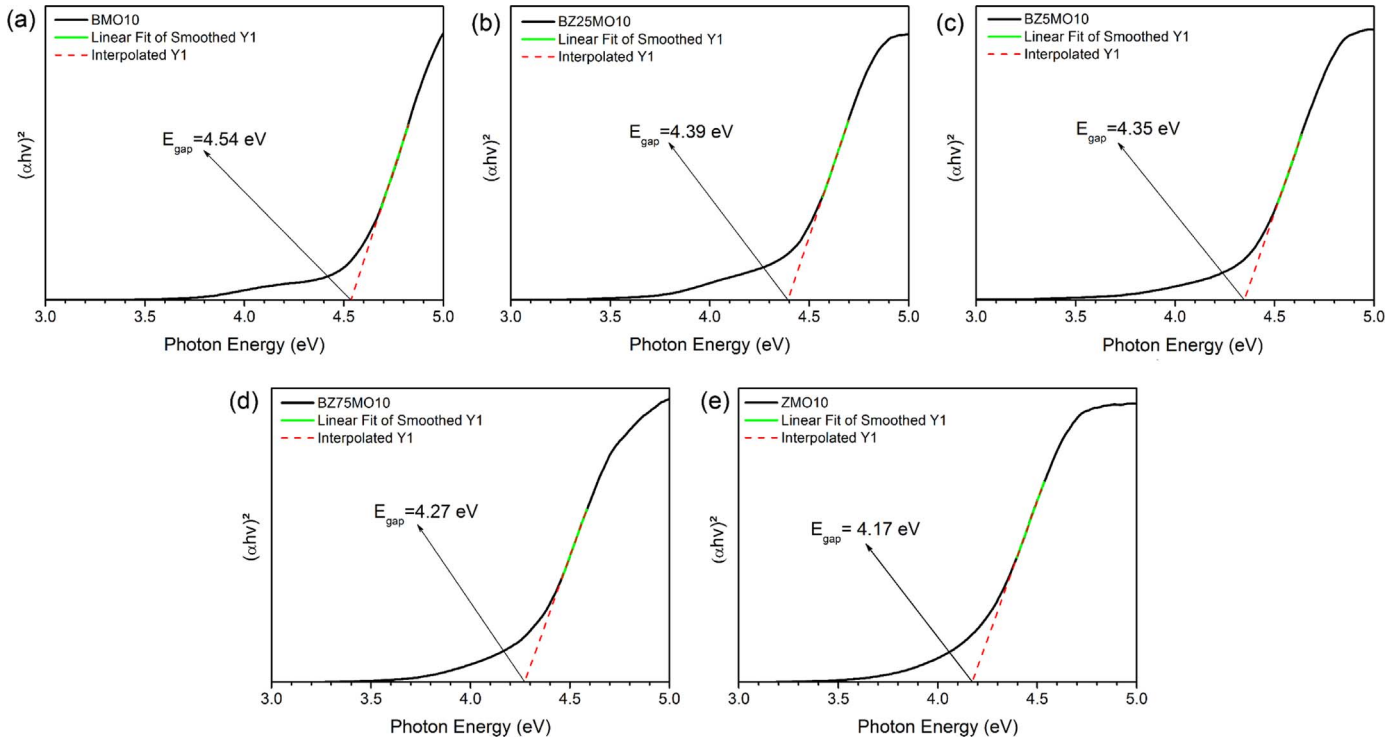

Fig. 6. UV–Vis absorbance spectra of (a) BMO10, (b) BZ25MO10, (c) BZ5MO10, (d) BZ75MO10 and (e) ZMO10.

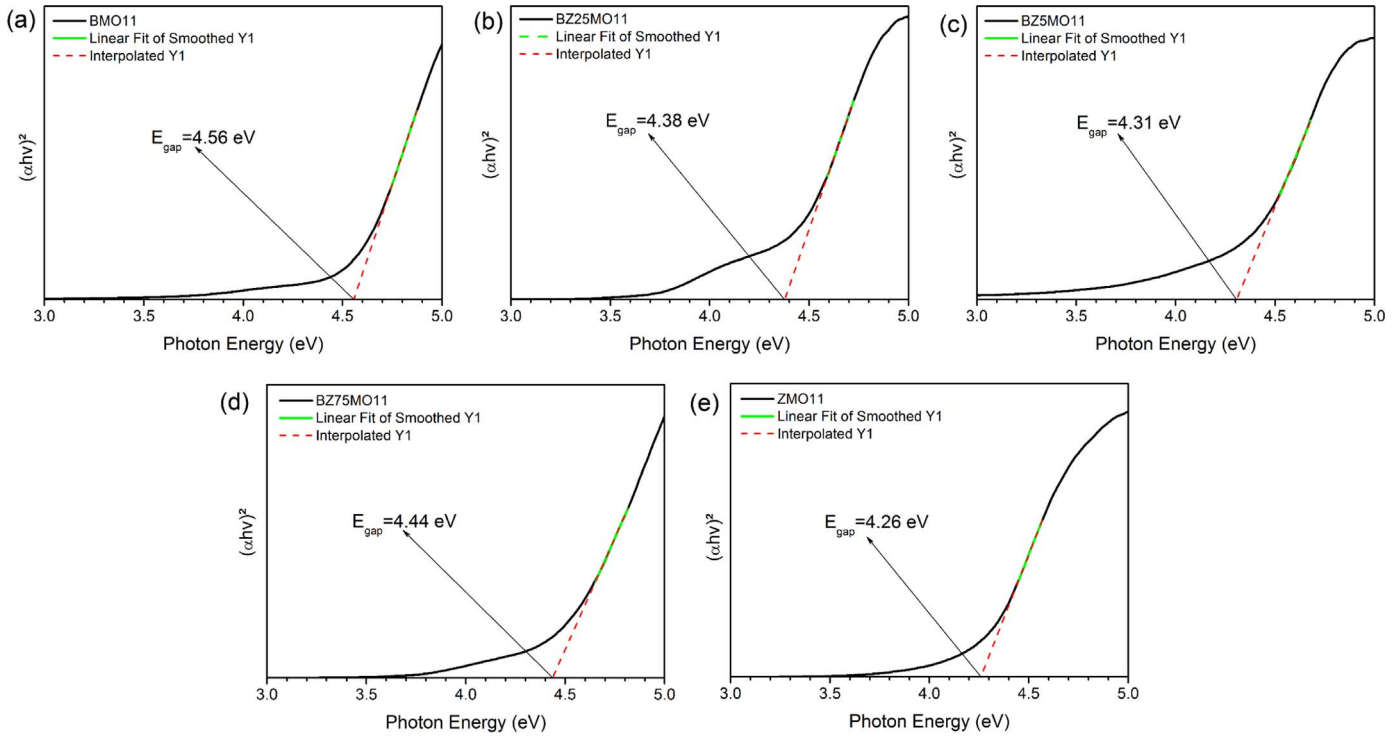

Fig. 7. UV–Vis absorbance spectra of (a) BMO11, (b) BZ25MO11, (c) BZ5MO11, (d) BZ75MO11 and (e) ZMO11.

the other hand, in Fig. 4i and j, ($ZnMoO_4$ microspheres formed by the USP process at 1000 °C and 1100 °C), it is seen that for the microspheres to be formed, an expressive number of primary particles is required, therefore, the primary particles present a much smaller particle size than the ones observed in Fig. 4a and b. This phenomenon can be explained by the difference in solubility of the barium and zinc precursor reagents. Messing et al. [60] described that solutes with a high degree of supersaturation tended to form a higher number of crystallites of nanometric sizes, whereas in solutes with a low degree of supersaturation, the formation of some large crystals occurred because the nucleation rate was small in relation to the growth rate. Therefore, as zinc nitrate presents solubility higher than barium nitrate, 120 g/100 g of H_2O and 10.3 g/100 g of H_2O, respectively [61], so the microspheres of the ZMO have smaller primary particles than BMO. Thus, by increasing the value of x in $Ba_{1-x}Zn_xMoO_4$, there is an increase in the densification of the microspheres and a decrease in the primary particle

Table 4
Comparative results between the E_{gap} values of de $Ba_{1-x}Zn_xMoO_4$ (x = 0; 0.25; 0.5; 0.75 and 1) obtained in this work and those reported in the literature.

Sample	E_{gap} (eV)	Synthesis method	Ref.
BMO10	4.54	USP	[This work]
BMO11	4.56	USP	[This work]
BZ25MO10	4.39	USP	[This work]
BZ25MO11	4.38	USP	[This work]
BZ5MO10	4.35	USP	[This work]
BZ5MO11	4.31	USP	[This work]
BZ75MO10	4.27	USP	[This work]
BZ75MO11	4.44	USP	[This work]
ZMO10	4.17	USP	[This work]
ZMO11	4.26	USP	[This work]
$BaMoO_4$	4.18	Mechanochemical	[65]
$BaMoO_4$	4.39	Polymeric precursor	[16]
$BaMoO_4$	4.33	Microwave-assisted hydrothermal	[16]
$ZnMoO_4$	4.30	Czochralski	[66]
$ZnMoO_4$	4.30	Czochralski	[67]

size for formation due to the solubility of the percussive reagents, as shown in Fig. 5.

It can be seen in Fig. 4(d-j) the formation of rod-like particles, most frequently when the temperature is at 1100 °C. It is believed that this fact occurs due to the ZMO having a melting temperature around 1000 °C [62], so spherical-like ZMO particles melt during the process and are recrystallized in rod format.

3.3. UV–Visible reflectance

Diffuse reflectance spectroscopy in the visible ultraviolet region was used to determine the gap band of the samples as a function of doping and temperature. The reflectance data were converted to absorbance data using the Kubelka-Munk function [63]. In order to estimate the value of the optical gap band (E_{gap}) it was used the Wood and Tauc method [64]. In this method, the optical gap energy is given by $\alpha h\nu \propto (h\nu - E_{gap})^k$, where h is the Planck constant, v is the frequency, α is the absorbance and k is indicated for the different transitions (k = 1/2, 2, 3/2 or 3 for direct permissible, indirect permissible, direct prohibited and indirect prohibited, respectively). For the $Ba_{1-x}Zn_xMoO_4$ samples, it was assumed k = 1/2, that is, direct permissible, indicating a direct permissible electronic transition. Graphs of absorbance versus photon energy (eV) were plotted and the linear portion of the curve was extrapolated for zero absorption in order to estimate E_{gap}. Figs. 6 and 7 and Table 4 shows the estimated values for E_{gap} of the samples of $Ba_{1-x}Zn_xMoO_4$ (x = 0, 0.25, 0.5, 0.75 and 1) at 1000 °C and 1100 °C.

The obtained values are in agreement with the values found in the literature, as shown in Table 4. The small changes in the gap energies can be related to the routes of synthesis used, as well as temperature, time, morphology and precursor reagents. The molybdates have few intermediate energy levels as a characteristic between the valence band and the conduction band, resulting in a high E_{gap} value, in which it is associated with the degree of structural order and disorder [16]. Thus, more ordered structures have higher gap energy values than structures with low order, because defects promote intermediate intervals between the conduction and valence bands, which reduces gap energy [22].

These intermediate intervals are usually associated with the formation of oxygen vacancies in the structure as a consequence of the rupture of symmetry among the bonds of the network forming atom and the oxygen [8]. It is assumed that the displacement of Mo atoms along the x, y and z axes promotes a redistribution of intermediate energy levels between the valence and conduction bands [68]. Other factors, such as polyhedron connectivity, of tetrahedra $[MoO_4]^{2-}$ distortion and mechanism growth, may be related to the E_{gap} of molybdates [69].

For the samples of $Ba_{1-x}Zn_xMoO_4$ with x = 0 there is higher gap energy, while for the samples with x = 1 the gap energy is lower. When the value of x = 0.25, 0.5 and 0.75, there is the formation of the tetragonal/triclinic heterostructure with the replacement of Zn^{2+} atoms by Ba^{2+} atoms in the triclinic lattice and replacement of Ba^{2+} atoms by Zn^{2+} atoms in the tetragonal lattice. The formation of the heterostructure and the atomic replacements will increase the degree of structural disorder of these samples, promoting a decrease in the gap energy. Thus, with the increase of the value of x, there is a decrease of the gap energy. As the temperature increases from 1000 °C to 1100 °C, a slight increase in the gap energy can be associated with the increase in the degree of structural ordering caused by the higher temperature.

3.4. Photoluminescence

Fig. 8 shows the PL emission spectra at room temperature of the $Ba_{1-x}Zn_xMoO_4$ (x = 0, 0.25, 0.5, 0.75 and 1) powders obtained by the USP method, when excited at 350.7 nm.

The results of the PL spectrum show that the samples have a behavior characteristic of a multiphonon and multilevel process, that is, a system in which the relaxation takes place in several ways and involves the participation of numerous states within the gap band of the material [70].

The disorder in materials can appear in different ways, such as vibration, rotation and orientation disorders (all referred to periodical materials) and topological disorder (in vitreous and amorphous materials). The PL spectroscopy is a powerful analysis of certain short-range feature of 2–5 Å and a medium range of 5–20 Å such as clusters in which the degree of local order is such that structurally unequal sites can be distinguished by their different types of electronic transitions and are linked to a specific structural arrangement [71].

There are several explanations in the literature that try to clarify the origin of PL properties of molybdates. Marques et al. [72] reported that the mixture of $[MoO_3]$ and $[MoO_4]$ clusters in molybdates was

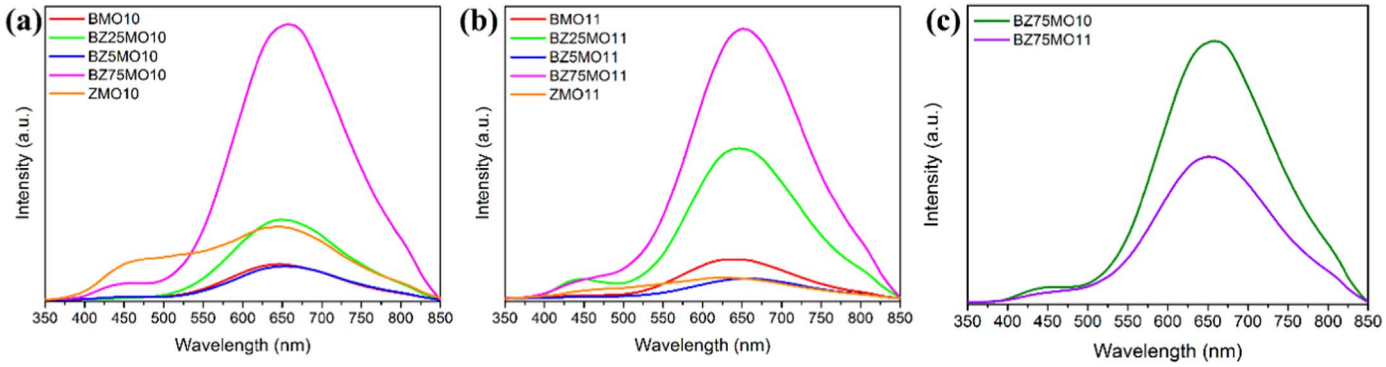

Fig. 8. PL emission spectra of $Ba_{1-x}Zn_xMoO_4$ (x = 0; 0,25; 0,5; 0,75 e 1) to (a) 1000 °C, (b) 1100 °C and (c) comparing the intensity of the PL emission between BZ75MO10 and BZ75MO11.

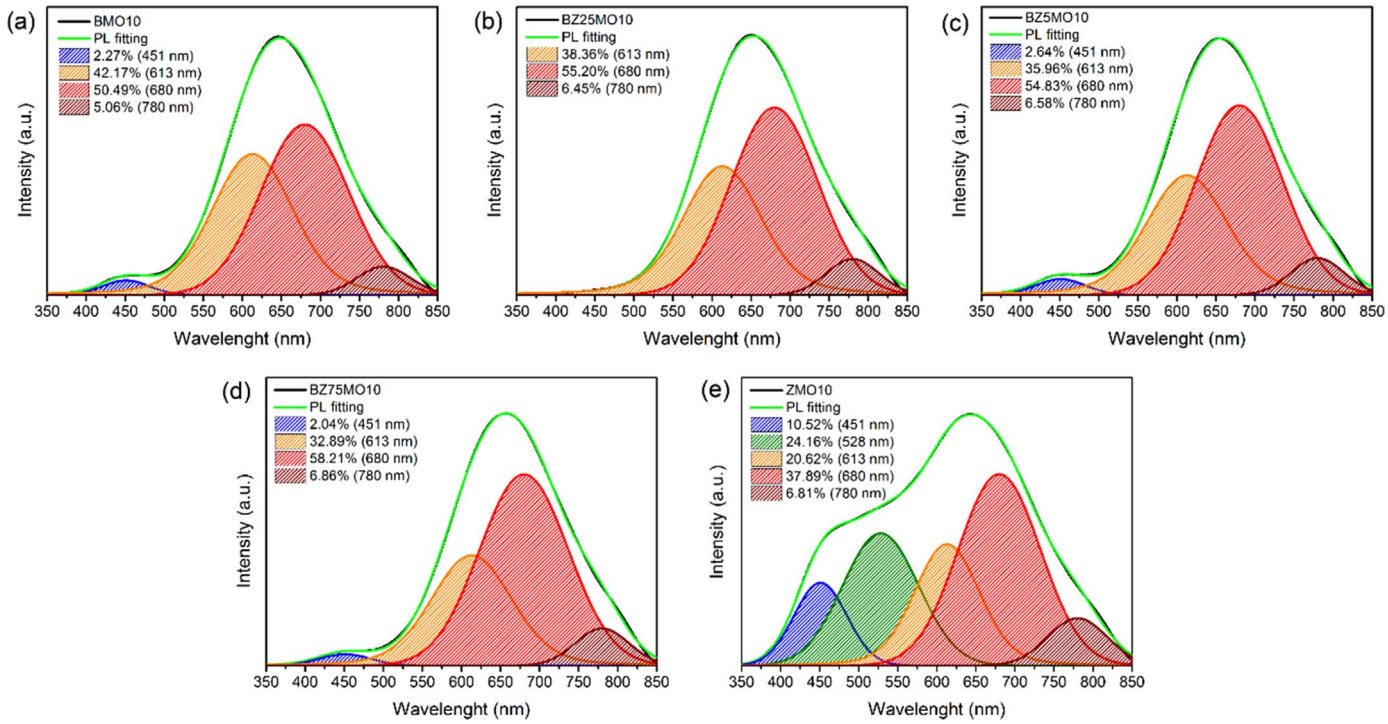

Fig. 9. Deconvolute the PL curves of (a) BMO10, (b) BZ25MO10, (c) BZ5MO10, (d) BZ75MO10 and (e) ZMO10.

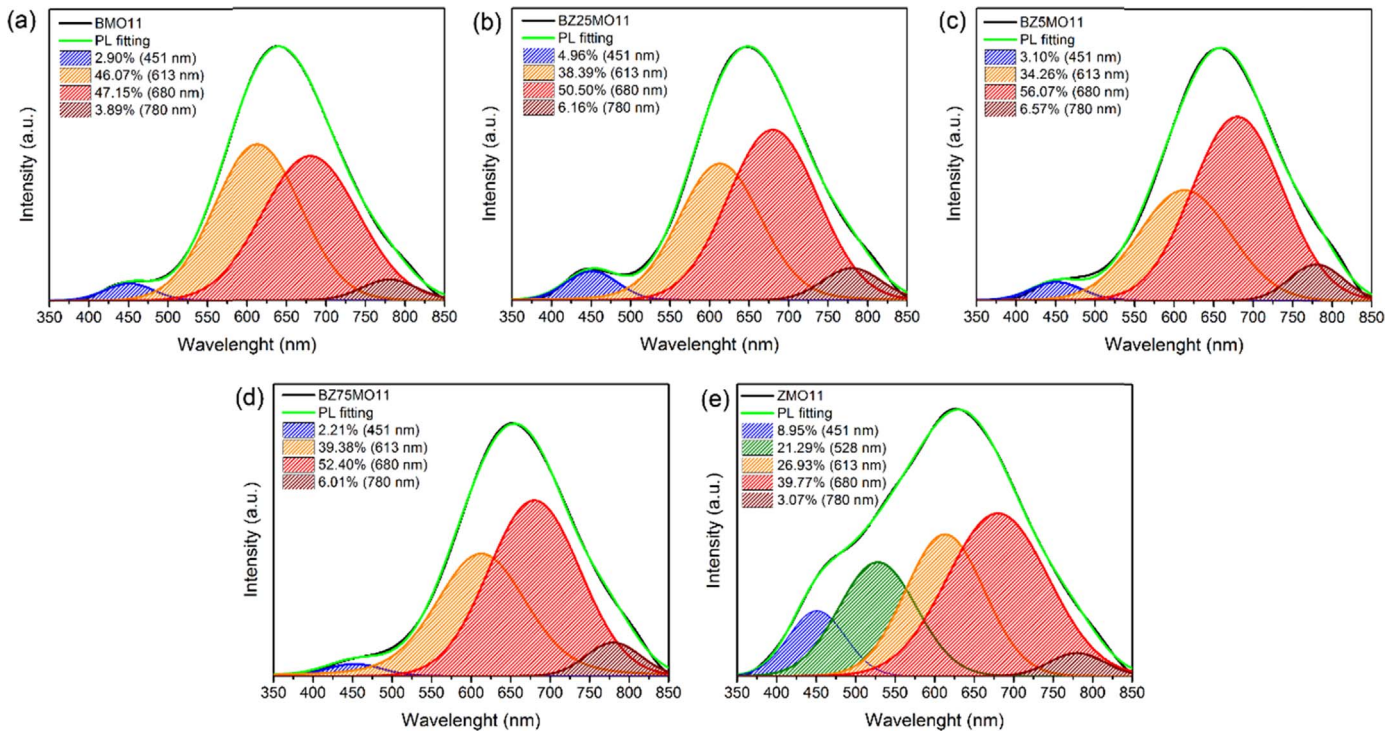

Fig. 10. Deconvolute the PL curves of (a) BMO11, (b) BZ25MO11, (c) BZ5MO11, (d) BZ75MO11 and (e) ZMO11.

responsible for the PL emission in the red region, whereas $[MoO_4]$ clusters were responsible for the emission in the blue. Wu et al. [73] considered that the emission band of the molybdates can be explained considering the Jahn-Teller active vibration modes of T_2 symmetry, which influence the complex anion $[MoO_4]^{2-}$ of slightly distorted tetrahedral symmetry, leading to a structured absorption band for the A1 → T1 (2) transition. Sung Lim [74] says that the emission spectrum of the molybdates is mainly due to the charge transfer transitions within the $[MoO_4]^{2-}$ complex and that the increase in crystallinity favors an increase in PL intensity. Marques et al. [75] describe the PL emission of molybdates as a result of the distortion of the tetrahedral complexes $[MoO_4]$, which promotes the existence of intermediate levels within the gap band, by the energy absorption of the 2p orbitals (lower energy state) of oxygen and the promotion of molybdenum 4d orbital (higher energy state), caused in the energy decay the participation of several states of energy. Longo et al. [76] report that vacancies in the oxygen

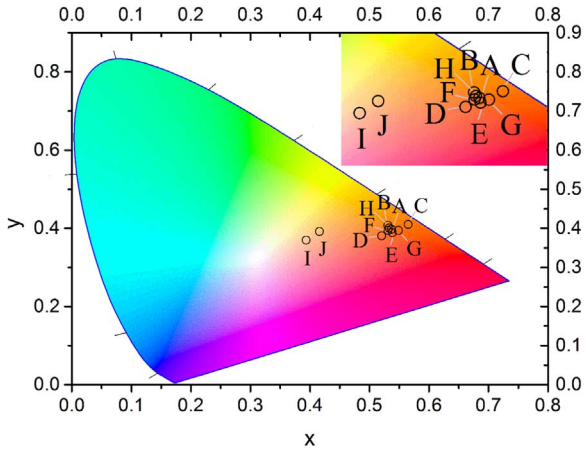

Fig. 11. CIE diagram of $Ba_{1-x}Zn_xMoO_4$ (x = 0, 0.25, 0.5, 0.75 and 1).

Table 5
Chromaticity coordinates (CIE) and correlated temperature color (CCT) for $Ba_{1-x}Zn_xMoO_4$ (x = 0, 0.25, 0.5, 0.75 and 1).

Code	Sample	x	y	CCT (K)	Color
A	BMO10	0.5371	0.3975	1825	Orange
B	BMO11	0.5307	0.4076	1933	Orange
C	BZ25MO10	0.5651	0.4096	1703	Orange
D	BZ25MO11	0.5205	0.3811	1850	Orange
E	BZ5MO10	0.5384	0.3887	1764	Orange
F	BZ5MO11	0.5313	0.3945	1850	Orange
G	BZ75MO10	0.5485	0.3943	1727	Orange
H	BZ75MO11	0.5328	0.4008	1876	Orange
I	ZMO10	0.3937	0.3698	3594	White
J	ZMO11	0.4160	0.3916	3282	White

complexes $[MoO_3{\bullet}V_o^x]$, $[MoO_3{\bullet}V_o^{\bullet}]$ and $[MoO_3{\bullet}V_o^{\bullet\bullet}]$ are deeply embedded in the gap band and are responsible for the PL emission in the red-yellow region of molybdates. It is believed that the molybdates PL emission to is given by the existence of intermediate levels within the gap band caused by the tetrahedral complex distortions $[MoO_4]$ [30,77–80].

Each electronic transition that occurs in PL is represented by a color and associated to a structural arrangement, the higher the degree of arrangement of this structural arrangement, the more the PL spectrum tends to increase in the areas of blue-green and decrease in the yellow-orange-red zones. Thus, the red-yellow emission is associated with a disordered structure with deep defects, whereas the blue-green emission is associated with an ordered structure with shallow defects [22].

Thus, when intermediate levels, represented by shallow and deep defects within the gap band of the material are excited, it occurs the electronic transition of the 2p oxygen orbitals in the valence band (VB) for 4d molybdenum orbitals by the absorption of (hv) by the conduction band (CB), resulting in the (hv') because of the radiative return of the electrons located in the 4d orbitals to the oxygen 2p orbitals [81].

In order to analyze the contribution of each color in the PL emission of the samples, the Gaussian curves obtained from the $Ba_{1-x}Zn_xMoO_4$ powders were carried out using the 4.12 PeakFit program and setting different wavelength values to obtain the secondary Gaussian curves. Figs. 9 and 10 shows these decompositions.

It can be seen that all samples have a predominance of PL emission in their red region. The samples with x ≤ 0.75 have smaller PL emission in the blue region, while the samples with x = 1, the emission in the blue and green regions is more intense. For x = 0, the PL emission in the red region is considered to be generated by the presence of vacancies in the $[MoO_4]$ complex that are associated with deep defects and for the blue region the emission is caused by the order-disorder of the $[BaO_8]$ complexes that are associated with shallow defects, as shown in the following equations:

$$[BaO_8]_o^X + [BaO_8]_d^X \rightarrow [BaO_8]_o' + [BaO_8]_d^{\bullet} \quad (1)$$

$$[MoO_4]^X + [MoO_3 \bullet V_o^{\bullet}]^X \rightarrow [MoO_4]' + [MoO_3 \bullet V_o^{\bullet}]' \quad (2)$$

For the samples with x = 1, the same reasoning is followed for the red region emission, but the emission in the blue and green regions is given by the order-disorder of the $[ZnO_6]$ complexes which are associated with shallow defects, as presented in the following equations:

$$[ZnO_6]_o^X + [ZnO_6]_d^X \rightarrow [ZnO_6]_o' + [ZnO_6]_d^{\bullet} \quad (3)$$

$$[MoO_4]^X + [MoO_3 \bullet V_o^{\bullet}]^X \rightarrow [MoO_4]' + [MoO_3 \bullet V_o^{\bullet}]' \quad (4)$$

For samples with x = 0.25, 0.5 and 0.75, it can be seen that the PL emission follows the same profile observed in the PL emission of the samples with x = 0. Thus, the PL emission of the $Ba_{1-x}Zn_xMoO_4$ heterostructure does not show emission intensity in the blue and green region as observed in the ZMO samples. It is believed that during the PL emission process the $[BaO_8]$ complex promotes the decrease in the deep defects of the $[ZnO_6]$ complex, as shown in the following equations:

$$[ZnO_6]_o^X + [ZnO_6]_d^X \rightarrow [ZnO_6]_o' + [ZnO_6]_d^{\bullet} \quad (5)$$

$$[BaO_8]_o^X + [BaO_8]_d^X \rightarrow [BaO_8]_o' + [BaO_8]_d^{\bullet} \quad (6)$$

$$[ZnO_6]_d' + [BaO_8]_d^{\bullet} \rightarrow [ZnO_6]_o^X + [BaO_8]_o^X \quad (7)$$

$$[ZnO_6]_d^{\bullet} + [BaO_8]_d' \rightarrow [ZnO_6]_o^X + [BaO_8]_o^X \quad (8)$$

$$[MoO_4]^X + [MoO_3 \bullet V_o^{\bullet}]^X \rightarrow [MoO_4]' + [MoO_3 \bullet V_o^{\bullet}]' \quad (9)$$

This event results from the resulting interface among the constituent structures of the heterostructure of $Ba_{1-x}Zn_xMoO_4$, promoting transfer of charges among them. If it is noticed that there is a decrease in the intensity of the PL emission with an increasing temperature, this phenomenon happens due to the increase of the structural ordering of the powders and as a consequence a decrease in the intermediate levels present in the gap band.

The light emission can be verified by determining the x and y coordinates. The CIE chromatic coordinates can be calculated by integrating the X, Y and Z values. The CIE is one of the important factors to evaluate the performance of phosphor. Fig. 11 shows the CIE (x, y) coordinates of the samples of $Ba_{1-x}Zn_xMoO_4$ (x = 0, 0.25, 0.5, 0.75 and 1), while Table 5 lists the CIE coordinates values, correlation color temperature (CCT) and the color emitted from each sample.

For the samples of $Ba_{1-x}Zn_xMoO_4$ with x ≤ 0.75, it is noticed the light emission in orange, whereas for the samples with x = 1 the emission was of white light. This is due to the fact that the samples with x ≤ 0.75 have a predominant PL emission spectrum in the orange-red region and little emission in the blue region. On the other hand, samples with x = 1 have a slightly predominant PL emission spectrum in the orange-red region and a relatively high contribution of the blue-green region. Some studies have been described the emission of molybdates in orange and white regions using rare earth elements in their composition [82–84]. On the other hand, with ultrasonic spray pyrolysis method it was able to produce $Ba_{1-x}Zn_xMoO_4$ with emission in orange and white regions without any rare earth elements.

4. Conclusion

The particles of $Ba_{1-x}Zn_xMoO_4$ (x = 0, 0.25, 0.5, 0.75 and 1) were successfully obtained by the ultrasonic pyrolysis spray method. This method presents several advantages against soft chemistry methods such as, simple method, low quantities of chemicals, obtaining particles continuously, not requiring further steps (such as annealing), and has prompt formation of particles inside of the reactor (≈ 1 min). On the other hand, spherical morphologies are easily obtained by ultrasonic spray pyrolysis without any surfactant during the synthesis.

The XRD patterns showed that samples with x = 0 have a scheelita tetragonal structure and the samples with x = 1 have a triclinic structure. While the samples with x = 0.25, 0.5 and 0.75 showed the formation of tetragonal/triclinic heterostructure. The adjacent particles showed predominantly spherical morphology, showing a decrease in the size of the primary forming particles with increasing x values, exhibiting a strong relation between the size of the primary particles and the solubility of the precursor reagents. The gap energy varies between 4.56 eV and 4.17 eV for x = 0 and x = 1, respectively, showing that the increase in the value of x raises the degree of disorder of the material, which will promote an increase of intermediate levels causing a decrease in the gap energy. The PL emission spectra of the samples have broadband behavior. The emission in the orange-red region was attributed to oxygen vacancies in the [MoO_4] cluster and the emission in the blue-green region was attributed to [BaO_8] and/or [ZnO_6] clusters. According to the CIE diagram, samples with x ≤ 0.75 and x = 1 shown a great emission in the orange and white regions, respectively, without using any earth rare element, which may be promising candidates for LED applications.

Acknowledgments

The authors thank the financial support from the following Brazilian research financing institutions: CNPq, (Processo 402127/2013-7), CAPES/PROCAD No. 2013/2998/2014, FAPESP (Processo 2013/07296-2) and Programa de Pós-Graduação em Ciência e Engenharia de Materiais (PPGCEM-UFRN) for their financial support.

Appendix A. Supplementary material

Supplementary data associated with this article can be found in the online version at http://dx.doi.org/10.1016/j.ceramint.2017.11.161.

References

[1] Y. Zhai, Y. Han, W. Zhang, Y. Yin, X. Zhao, J. Wang, X. Liu, Influence of doping alkali metal ions on the structure and luminescent properties of microwave synthesized CaMoO4:Dy3+ phosphors, J. Alloy. Compd. 688 (Part A) (2016) 241–247.
[2] P. Madhusudan, J. Zhang, J. Yu, B. Cheng, D. Xu, J. Zhang, One-pot template-free synthesis of porous CdMoO4 microspheres and their enhanced photocatalytic activity, Appl. Surf. Sci. 387 (2016) 202–213.
[3] Y. Yin, Y. Li, H. Zhang, F. Ren, D. Zhang, W. Feng, L. Shao, K. Li, Y. Liu, Z. Sun, M. Li, G. Song, G. Wang, One-step fabrication of BaMoO4 microstructures with controlled morphologies via a simple EDTA-mediated route, Superlattices Microstruct. 55 (2013) 109–117.
[4] K.J. Samdani, J.S. Samdani, N.H. Kim, J.H. Lee, FeMoO4 based, enzyme-free electrochemical biosensor for ultrasensitive detection of norepinephrine, Biosens. Bioelectron. 81 (2016) 445–453.
[5] J.L. Wu, B.S. Cao, F. Lin, B.J. Chen, J.S. Sun, B. Dong, A new molybdate host material: synthesis, upconversion, temperature quenching and sensing properties, Ceram. Int. 42 (2016) 18666–18673.
[6] S.-H. Liao, S.-Y. Lu, S.-J. Bao, Y.-N. Yu, M.-Q. Wang, NiMoO4 nanofibres designed by electrospining technique for glucose electrocatalytic oxidation, Anal. Chim. Acta 905 (2016) 72–78.
[7] E.S. Kim, C.J. Jeon, P.G. Clem, Effects of crystal structure on the microwave dielectric properties of ABO4 (A = Ni, Mg, Zn and B = Mo, W) ceramics, J. Am. Ceram. Soc. 95 (2012) 2934–2938.
[8] J.C. Sczancoski, L.S. Cavalcante, N.L. Marana, R.O. da Silva, R.L. Tranquilin, M.R. Joya, P.S. Pizani, J.A. Varela, J.R. Sambrano, M. Siu Li, E. Longo, J. Andrés, Electronic structure and optical properties of BaMoO4 powders, Curr. Appl. Phys. 10 (2010) 614–624.
[9] Y. Sun, J. Ma, J. Fang, C. Gao, Z. Liu, Synthesis of BaMoO4 high photoluminescent whiskers by an electrochemical method, Ceram. Int. 37 (2011) 683–686.
[10] X. Nie, W. Wulayin, T. Song, M. Wu, X. Qiao, Surface, optical characteristics and photocatalytic ability of Scheelite-type monoclinic Bi3FeMo2O12 nanoparticles, Appl. Surf. Sci. 387 (2016) 351–357.
[11] H. Ait ahsaine, M. Zbair, M. Ezahri, A. Benlhachemi, M. Arab, B. Bakiz, F. Guinneton, J.R. Gavarri, Rietveld refinements, impedance spectroscopy and phase transition of the polycrystalline ZnMoO4 ceramics, Ceram. Int. 41 (2015) 15193–15201.
[12] M. Buryi, D.A. Spassky, J. Hybler, V. Laguta, M. Nikl, Electron spin resonance study of charge trapping in α-ZnMoO4 single crystal scintillator, Opt. Mater. 47 (2015) 244–250.
[13] Y.-R. Jiang, W.W. Lee, K.-T. Chen, M.-C. Wang, K.-H. Chang, C.-C. Chen, Hydrothermal synthesis of β-ZnMoO4 crystals and their photocatalytic degradation of Victoria Blue R and phenol, J. Taiwan Inst. Chem. Eng. 45 (2014) 207–218.
[14] L.S. Cavalcante, J.C. Sczancoski, M. Siu Li, E. Longo, J.A. Varela, β-ZnMoO4 microcrystals synthesized by the surfactant-assisted hydrothermal method: growth process and photoluminescence properties, Colloids Surf. A: Physicochem. Eng. Asp. 396 (2012) 346–351.
[15] X. Ma, W. Zhao, J. Wu, X. Jia, Preparation of flower-like BaMoO4 and application in rechargeable lithium and sodium ion batteries, Mater. Lett. 188 (2017) 248–251.
[16] L.D.S. Alencar, A. Mesquita, C.A.C. Feitosa, R. Balzer, L.F.D. Probst, D.C. Batalha, M.G. Rosmaninho, H.V. Fajardo, M.I.B. Bernardi, Preparation, characterization and catalytic application of Barium molybdate (BaMoO4) and Barium tungstate (BaWO4) in the gas-phase oxidation of toluene, Ceram. Int. 43 (2017) 4462–4469.
[17] D.L. Guo, Q. Yang, H. Hua, C.G. Hu, Room temperature ferromagnetism in shuttle-like BaMoO4 microcrystals, J. Phys. Chem. C 118 (2014) 13826–13832.
[18] J. Fei, Q. Sun, J. Li, Y. Cui, J. Huang, W. Hui, H. Hu, Synthesis and electrochemical performance of α-ZnMoO4 nanoparticles as anode material for lithium ion batteries, Mater. Lett. 198 (2017) 4–7.
[19] D. Spassky, V. Nagirnyi, S. Vielhauer, H. Mägi, S.G. Nasonov, V.N. Shlegel, A. Belsky, Emission centers in ZnMoO4: influence of growth conditions and decay characteristics, Opt. Mater. 59 (2016) 66–69.
[20] D.V. Poda, Scintillating bolometers based on ZnMoO4 and Zn100MoO4 crystals to search for 0ν2β decay of 100Mo (LUMINEU project): first tests at the modane underground laboratory, Nucl. Part. Phys. Proc. 273–275 (2016) 1801–1806.
[21] D.M. Chernyak, F.A. Danevich, V.Y. Degoda, A. Giuliani, I.M. Ivanov, Y.P. Kogut, H. Kraus, B.N. Kropivyansky, E.P. Makarov, M. Mancuso, P. de Marcillac, V.B. Mikhailik, V.M. Mokina, I.M. Moroz, S.G. Nasonov, O. Plantevin, D.V. Poda, V.N. Shlegel, M. Tenconi, V.I. Tretyak, M. Velazquez, V.N. Zhdankov, Effect of tungsten doping on ZnMoO4 scintillating bolometer performance, Opt. Mater. 49 (2015) 67–74.
[22] M.F.C. Abreu, F.V. Motta, R.C. Lima, M.S. Li, E. Longo, A.Pd.A. Marques, Effect of process parameters on photophysical properties and barium molybdate phosphors characteristics, Ceram. Int. 40 (2014) 6719–6729.
[23] D. Hu, Y. Wang, W. Huan, Structural and photoluminescent properties of BaxZn1−xMoO4:Eu3+ phosphors synthesized by solid-state reaction method, J. Mater. Sci.: Mater. Electron. 26 (2015) 1311–1315.
[24] B.-G. Zhai, Q.-l. Ma, L. Yang, Y.M. Huang, Growth of ZnMoO4 nanowires via vapor deposition in air, Mater. Lett. 188 (2017) 119–122.
[25] V.Y. Degoda, Y.P. Kogut, I.M. Moroz, F.A. Danevich, Long time phosphorescence in ZnMoO4 crystals, J. Lumin. 181 (2017) 269–276.
[26] T. Chengaiah, C.K. Jayasankar, K. Pavani, T. Sasikala, L.R. Moorthy, Preparation and luminescence characterization of Zn(1−x)MoO4: xDy3+ phosphor for white light-emitting diodes, Opt. Commun. 312 (2014) 233–237.
[27] C. Bouzidi, M. Ferhi, H. Elhouichet, M. Ferid, Structural and luminescence properties of (Ba1−xEux)MoO4 powders, J. Lumin. 179 (2016) 230–235.
[28] C. Shivakumara, R. Saraf, S. Behera, N. Dhananjaya, H. Nagabhushana, Synthesis of Eu3+-activated BaMoO4 phosphors and their Judd–Ofelt analysis: applications in lasers and white LEDs, Spectrochim. Acta Part A: Mol. Biomol. Spectrosc. 151 (2015) 141–148.
[29] P. Jena, S.K. Gupta, V. Natarajan, O. Padmaraj, N. Satyanarayana, M. Venkateswarlu, On the photo-luminescence properties of sol–gel derived undoped and Dy3+ ion doped nanocrystalline Scheelite type AMoO4 (A = Ca, Sr and Ba), Mater. Res. Bull. 64 (2015) 223–232.
[30] M. Ghaed-Amini, M. Bazarganipour, M. Salavati-Niasari, K. Saberyan, Morphology and photoluminescence of BaMoO4 micro- and nano-crystals synthesized by co-precipitation method, Trans. Nonferrous Met. Soc. China 25 (2015) 3967–3973.
[31] A.K. Soni, A. Kumari, V.K. Rai, Optical investigation in shuttle like BaMoO4:Er3+–Yb3+ phosphor in display and temperature sensing, Sens. Actuators B: Chem. 216 (2015) 64–71.
[32] Z. Shahri, M. Bazarganipour, M. Salavati-Niasari, Controllable synthesis of novel zinc molybdate rod-like nanostructures via simple surfactant-free precipitation route, Superlattices Microstruct. 63 (2013) 258–266.
[33] M. Lei, C.X. Ye, S.S. Ding, K. Bi, H. Xiao, Z.B. Sun, D.Y. Fan, H.J. Yang, Y.G. Wang, Controllable route to barium molybdate crystal and their photoluminescence, J. Alloy. Compd. 639 (2015) 102–105.
[34] W. Zhang, J. Yin, F. Min, L. Jia, D. Zhang, Q. Zhang, J. Xie, Preparation and photoluminescence properties of MMoO4 (M = Cu, Ni, Zn) nano-particles synthesized via electrolysis, J. Mol. Struct. 1127 (2017) 777–783.
[35] Z. Li, Y. Wang, J. Cao, Y. Jiang, X. Zhao, Z. Meng, Hydrothermal synthesis and luminescent properties of BaMoO4:Sm3+ red phosphor, J. Rare Earths 34 (2016) 143–147.
[36] C. Zhang, L. Zhang, C. Song, G. Jia, S. Huo, S. Shen, Well-defined barium molybdate hierarchical architectures with different morphologies: controllable synthesis, formation process, and luminescence properties, J. Alloy. Compd. 589 (2014) 185–191.
[37] Y. Keereeta, T. Thongtem, S. Thongtem, Effect of medium solvent ratios on morphologies and optical properties of α-ZnMoO4, β-ZnMoO4 and ZnMoO4·0.8H2O crystals synthesized by microwave-hydrothermal/solvothermal method, Superlattices Microstruct. 69 (2014) 253–264.
[38] M. Bazarganipour, Synthesis and characterization of BaMoO4 nanostructures prepared via a simple sonochemical method and their degradation ability of methylene blue, Ceram. Int. 42 (2016) 12617–12622.
[39] S.E. Karekar, B.A. Bhanvase, S.H. Sonawane, M.P. Deosarkar, D.V. Pinjari, A.B. Pandit, Synthesis of zinc molybdate and zinc phosphomolybdate nanopigments by an ultrasound assisted route: advantage over conventional method, Chem. Eng. Process.: Process Intensif. 87 (2015) 51–59.
[40] T. Li, X. Li, Z. Wang, H. Guo, W. Peng, K. Zeng, Electrochemical properties of LiNi0.6Co0.2Mn0.2O2 as cathode material for Li-ion batteries prepared by

ultrasonic spray pyrolysis, Mater. Lett. 159 (2015) 39–42.
[41] H. Choi, D. Kim, S.P. Yoon, J. Han, S. Ha, J. Kim, Production of molybdenum oxide particles with high yield by ultrasonic spray pyrolysis and their catalytic activity toward partial oxidation of n-dodecane, J. Anal. Appl. Pyrolysis 112 (2015) 276–283.
[42] N. Shatrova, A. Yudin, V. Levina, E. Dzidziguri, D. Kuznetsov, N. Perov, J.-P. Issi, Elaboration, characterization and magnetic properties of cobalt nanoparticles synthesized by ultrasonic spray pyrolysis followed by hydrogen reduction, Mater. Res. Bull. 86 (2017) 80–87.
[43] Y.H. Cho, X. Liang, Y.C. Kang, J.-H. Lee, Ultrasensitive detection of trimethylamine using Rh-doped SnO2 hollow spheres prepared by ultrasonic spray pyrolysis, Sens. Actuators B: Chem. 207 (Part A) (2015) 330–337.
[44] B. Ebin, G. Lindbergh, S. Gürmen, Preparation and electrochemical properties of nanocrystalline LiBxMn2−xO4 cathode particles for Li-ion batteries by ultrasonic spray pyrolysis method, J. Alloy. Compd. 620 (2015) 399–406.
[45] B. Ebin, S. Gürmen, G. Lindbergh, Preparation and electrochemical properties of spinel LiFexCuyMn1.2O4 by ultrasonic spray pyrolysis, Ceram. Int. 40 (2014) 1019–1027.
[46] H. Das, N. Sakamoto, H. Aono, K. Shinozaki, H. Suzuki, N. Wakiya, Investigations of superparamagnetism in magnesium ferrite nano-sphere synthesized by ultrasonic spray pyrolysis technique for hyperthermia application, J. Magn. Magn. Mater. 392 (2015) 91–100.
[47] A. Yudin, N. Shatrova, B. Khaydarov, D. Kuznetsov, E. Dzidziguri, J.-P. Issi, Synthesis of hollow nanostructured nickel oxide microspheres by ultrasonic spray atomization, J. Aerosol Sci. 98 (2016) 30–40.
[48] T. Li, X. Li, Z. Wang, H. Guo, Q. Hu, W. Peng, Synthesis of nanoparticles-assembled Co3O4 microspheres as anodes for Li-ion batteries by spray pyrolysis of CoCl2 solution, Electrochim. Acta 209 (2016) 456–463.
[49] Y. Huang, Y. Gao, Q. Zhang, J.-j. Cao, R.-j. Huang, W. Ho, S.C. Lee, Hierarchical porous ZnWO4 microspheres synthesized by ultrasonic spray pyrolysis: characterization, mechanistic and photocatalytic NOx removal studies, Appl. Catal. A: General. 515 (2016) 170–178.
[50] M.T.S. Tavares, M.M. Melo, V.D. Araújo, R.L. Tranquilin, C.R.R. Almeida, C.A. Paskocimas, M.R.D. Bomio, E. Longo, F.V. Motta, Enhancement of the photocatalytic activity and white emission of CaIn2O4 nanocrystals, J. Alloy. Compd. 658 (2016) 316–323.
[51] C. Goulart, E. Djurado, Synthesis and sintering of Gd-doped CeO2 nanopowders prepared by ultrasonic spray pyrolysis, J. Eur. Ceram. Soc. 33 (2013) 769–778.
[52] T. Hyodo, E. Fujii, K. Ishida, T. Ueda, Y. Shimizu, Microstructural control of porous In2O3 powders prepared by ultrasonic-spray pyrolysis employing self-synthesized polymethylmethacrylate microspheres as a template and their NO2-sensing properties, Sens. Actuators B: Chem. 244 (2017) 992–1003.
[53] Y.H. Cho, Y.N. Ko, Y.C. Kang, I.-D. Kim, J.-H. Lee, Ultraselective and ultrasensitive detection of trimethylamine using MoO3 nanoplates prepared by ultrasonic spray pyrolysis, Sens. Actuators B: Chem. 195 (2014) 189–196.
[54] Y. Li, X. Li, Z. Wang, H. Guo, T. Li, Distinct impact of cobalt salt type on the morphology, microstructure, and electrochemical properties of Co3O4 synthesized by ultrasonic spray pyrolysis, J. Alloy. Compd. 696 (2017) 836–843.
[55] C.R.R. Almeida, L.X. Lovisa, A.A.G. Santiago, M.S. Li, E. Longo, C.A. Paskocimas, F.V. Motta, M.R.D. Bomio, One-step synthesis of CaMoO4: Eu3+ nanospheres by ultrasonic spray pyrolysis, J. Mater. Sci.: Mater. Electron. (2017).
[56] H. Rietveld, A profile refinement method for nuclear and magnetic structures, J. Appl. Crystallogr. 2 (1969) 65–71.
[57] B. Toby, EXPGUI, a graphical user interface for GSAS, J. Appl. Crystallogr. 34 (2001) 210–213.
[58] R. Shannon, Revised effective ionic radii and systematic studies of interatomic distances in halides and chalcogenides, Acta Crystallogr. Sect. A 32 (1976) 751–767.
[59] K. Momma, F. Izumi, VESTA 3 for three-dimensional visualization of crystal, volumetric and morphology data, J. Appl. Crystallogr. 44 (2011) 1272–1276.
[60] G.L. Messing, S.-C. Zhang, G.V. Jayanthi, Ceramic powder synthesis by spray pyrolysis, J. Am. Ceram. Soc. 76 (1993) 2707–2726.
[61] D.R. Lide, CRC Handbook of Chemistry and Physics, 85th ed., Taylor & Francis, 2004.
[62] L.I. Ivleva, I.S. Voronina, L.Y. Berezovskaya, P.A. Lykov, V.V. Osiko, L.D. Iskhakova, Growth and properties of ZnMoO4 single crystals, Crystallogr. Rep. 53 (2008) 1087–1090.
[63] L. Tolvaj, K. Mitsui, D. Varga, Validity limits of Kubelka–Munk theory for DRIFT spectra of photodegraded solid wood, Wood Sci. Technol. 45 (2011) 135–146.
[64] D.L. Wood, J. Tauc, Weak absorption tails in amorphous semiconductors, Phys. Rev. B 5 (1972) 3144–3151.
[65] W. Janbua, T. Bongkarn, W. Vittayakorn, N. Vittayakorn, Direct synthesis and growth mechanism of metal molybdate (AMoO4; A = Ca and Ba) fine particles via the mechanochemical method, Ceram. Int. 43 (2017) S435–S443.
[66] D.A. Spassky, N.S. Kozlova, V. Nagirnyi, A.E. Savon, Y.A. Hizhnyi, S.G. Nedilko, Excitation energy transfer to luminescence centers in MIIMoO4 (MII = Ca, Sr, Zn, Pb) and Li2MoO4, J. Lumin. 186 (2017) 229–237.
[67] D.A. Spassky, A.N. Vasil'ev, I.A. Kamenskikh, V.V. Mikhailin, A.E. Savon, A.H. Yu, S.G. Nedilko, P.A. Lykov, Electronic structure and luminescence mechanisms in ZnMoO 4 crystals, J. Phys.: Condens. Matter 23 (2011) 365501.
[68] G. Botelho, I.C. Nogueira, E. Moraes, E. Longo, Study of structural and optical properties of CaMoO4 nanoparticles synthesized by the microwave-assisted solvothermal method, Mater. Chem. Phys. 183 (2016) 110–120.
[69] T. Thongtem, S. Kungwankunakorn, B. Kuntalue, A. Phuruangrat, S. Thongtem, Luminescence and absorbance of highly crystalline CaMoO4, SrMoO4, CaWO4 and SrWO4 nanoparticles synthesized by co-precipitation method at room temperature, J. Alloy. Compd. 506 (2010) 475–481.
[70] V.M. Longo, L.S. Cavalcante, A.T. de Figueiredo, L.P.S. Santos, E. Longo, J.A. Varela, J.R. Sambrano, C.A. Paskocimas, F.S. De Vicente, A.C. Hernandes, Highly intense violet-blue light emission at room temperature in structurally disordered SrZrO3 powders, Appl. Phys. Lett. 90 (2007) 091906.
[71] V.M. Longo, L.S. Cavalcante, E.C. Paris, J.C. Sczancoski, P.S. Pizani, M.S. Li, J. Andrés, E. Longo, J.A. Varela, Hierarchical assembly of CaMoO4 nano-octahedrons and their photoluminescence properties, J. Phys. Chem. C 115 (2011) 5207–5219.
[72] A.Pd.A. Marques, D.M.A. de Melo, C.A. Paskocimas, P.S. Pizani, M.R. Joya, E.R. Leite, E. Longo, Photoluminescent BaMoO4 nanopowders prepared by complex polymerization method (CPM), J. Solid State Chem. 179 (2006) 671–678.
[73] X. Wu, J. Du, H. Li, M. Zhang, B. Xi, H. Fan, Y. Zhu, Y. Qian, Aqueous mineralization process to synthesize uniform shuttle-like BaMoO4 microcrystals at room temperature, J. Solid State Chem. 180 (2007) 3288–3295.
[74] C. Sung Lim, Microwave-assisted synthesis and photoluminescence of MMoO4 (M = Ca, Ba) particles via a metathetic reaction, J. Lumin. 132 (2012) 1774–1780.
[75] V.S. Marques, L.S. Cavalcante, J.C. Sczancoski, A.F.P. Alcântara, M.O. Orlandi, E. Moraes, E. Longo, J.A. Varela, M. Siu Li, M.R.M.C. Santos, Effect of different solvent ratios (water/ethylene glycol) on the growth process of CaMoO4 crystals and their optical properties, Cryst. Growth Des. 10 (2010) 4752–4768.
[76] V.M. Longo, A.Td Figueiredo, A.B. Campos, J.W.M. Espinosa, A.C. Hernandes, C.A. Taft, J.R. Sambrano, J.A. Varela, E. Longo, Different origins of green-light photoluminescence emission in structurally ordered and disordered powders of calcium molybdate, J. Phys. Chem. A 112 (2008) 8920–8928.
[77] Y.-F. Liu, L.-l. Xia, Y.-N. Lu, S.-H. Dai, M. Takeguchi, H.-M. Hong, Z.-G. Pan, Surfactant-free microwave-assisted hydrothermal synthesis of BaMoO4 hierarchical self-assemblies and enhanced photoluminescence properties, J. Colloid Interface Sci. 381 (2012) 24–29.
[78] Y. Mi, Z. Huang, F. Hu, X. Li, Room temperature reverse-microemulsion synthesis and photoluminescence properties of uniform BaMoO4 submicro-octahedra, Mater. Lett. 63 (2009) 742–744.
[79] M. Li, Y. Guan, Y. Yin, X. Cui, S. Rong, G. Jin, Y. Hao, Q. Wu, Controllable synthesis of 3D BaXO4 (X = W, Mo) microstructures by adjusting nucleation stage and their photoluminescence properties, Superlattices Microstruct. 80 (2015) 222–228.
[80] Y. Yin, Z. Gan, Y. Sun, B. Zhou, X. Zhang, D. Zhang, P. Gao, Controlled synthesis and photoluminescence properties of BaXO4 (X = W, Mo) hierarchical nanostructures via a facile solution route, Mater. Lett. 64 (2010) 789–792.
[81] G.M. Gurgel, L.X. Lovisa, O.L.A. Conceição, M.S. Li, E. Longo, C.A. Paskocimas, F.V. Motta, M.R.D. Bomio, Evaluation of morphology and photoluminescent properties of PbMoO4 crystals by ultrasonic amplitude, J. Mater. Sci. 52 (2017) 4608–4620.
[82] C. Zhang, L. Zhang, C. Song, G. Jia, S. Huo, S. Shen, Well-defined barium molybdate hierarchical architectures with different morphologies: controllable synthesis, formation process, and luminescence properties, J. Alloy. Compd. 589 (2014) 185–191.
[83] J. Zhang, R. Li, L. Liu, L. Li, L. Zou, S. Gan, G. Ji, Self-assembled 3D sphere-like SrMoO4 and SrMoO4:Ln3+ (Ln = Eu, Sm, Tb, Dy) microarchitectures: facile sonochemical synthesis and optical properties, Ultrason. Sonochem. 21 (2014) 1736–1744.
[84] Z. Hou, R. Chai, M. Zhang, C. Zhang, P. Chong, Z. Xu, G. Li, J. Lin, Fabrication and luminescence properties of one-dimensional CaMoO4: Ln3+ (Ln = Eu, Tb, Dy) nanofibers via electrospinning process, Langmuir 25 (2009) 12340–12348.